SPE-185590-MS

Integrated Modeling of Formation Damage and Multiple Induced Hydraulic Fractures During Produced Water Reinjection

K. Fischer, F. C. Ferreira, B. B. Holzberg, and J. S. Pastor, Schlumberger; L. Reinli, R. Furuie, D. M. Vasconcelos, and T. A. Dutra, Statoil

This paper was prepared for presentation at the SPE Latin America and Caribbean Petroleum Engineering Conference held in Buenos Aires, Argentina, 18-19 May 2017.

Abstract

During produced water reinjection into an oilfield, the formation near the wellbore is progressively damaged due to total suspended solids (TSS) and oil particles in the injected water (OIW). This typically increases the bottom-hole injection pressure over time. Furthermore, if the water is injected in the oil zone, the initial bottom-hole injection pressure may already be high from the start due to water mobility constraint and oil viscosity. This study aims to model the generation of hydraulic fractures induced under different conditions, their geometrical characteristics and corresponding development over time. Such information is key to reservoir simulation for the secondary oil recovery and to reservoir integrity assessment.

Four disciplines are integrated into the proposed workflow: reservoir flow simulation, formation damage modeling, reservoir geomechanics, and the simulation of hydraulic fracturing. First, a sector model around an injector well is extracted from the full-field reservoir simulation of the case-study reservoir. In the reservoir flow simulation, a formation damage model is implemented, calibrated from injection rate, bottom-hole pressure, TSS and OIW actual data. At specified time steps, the flow simulator passes pore pressure profiles of the sector model to the geomechanical simulator, which computes the corresponding changes in stress and deformation.

The updated in-situ stress field, in combination with the petrophysical model applied for the flow simulation, is provided to the hydraulic fracturing simulator, which tests for the development of the hydraulic fracture and computes its geometry. The resulting hydraulic fracture is mapped back into the reservoir flow model to account for the local increase of permeability of the cells hosting the fracture. The workflow then enters into a loop starting again with the flow simulation, and the further development of the fracture under changing conditions is tested and modeled.

The proposed workflow was successfully applied to an injection well in an offshore field. Four scenarios considered different initial formation saturation, injected fluid viscosity and the conversion of a producing well into an injector. Multiple fractures with different characteristics, fully contained inside the reservoir, were predicted for each scenario and gave insights into the hydraulic fracture development during produced water reinjection.

The proposed method and workflow have the potential to significantly improve the reservoir simulation of the water injection process for secondary recovery or pressure maintenance by providing insights into how induced fracture geometries will influence the injection pressure and reservoir sweep efficiency. It also may provide valuable information to assess the integrity of reservoir cap rock during produced water reinjection.

Introduction

In order to model and analyze hydraulic fracture development during produced water reinjection, four disciplines are integrated into an end-to-end workflow: reservoir flow simulation, formation damage modeling, reservoir geomechanics, and the simulation of hydraulic fracturing. The proposed workflow was applied to a field located offshore Brazil. The reservoir is a typical heterogeneous turbidity system formed by deposition of gravity flows from deltaic and shallow marine systems. It consists of poorly consolidated sandstones sealed by shale formations. The reservoir contains heavy oil (14° API), with moderate aquifer support and no gas cap. The field exploitation is done through several long horizontal wells, supported by artificial lift. A quick pore pressure drop is expected, which has been balanced by water injection. Injected water, as well as water from the aquifer, is quickly produced in large amounts through the producing wells due to the unfavorable oil-water mobility ratio. Due to offshore limitations to water management, produced water reinjection is a key strategy, providing pressure support for reservoir management and water disposal. All produced water is planned to be re-injected in this field.

In the oil and gas industry in general, a significant volume of water is typically produced along with hydrocarbons. The reinjection of produced water is usually applied to safely discard it according to environmental and legal requirements, and also to maintain the reservoir pressure and enhance the oil recovery through water flooding. Due to the water production and separation processes, the reinjected water usually contains residual oil droplets (oil in water, OIW) and small solid particles (total suspended solids, TSS). Such water impurities may significantly reduce the formation permeability and impair the well injectivity, consequently reducing the injection rates or increasing the bottom-hole pressure (BHP). Such permeability damage may be restricted to the wellbore wall through the formation of a filter cake at the sand face, but the particles may also filter inwards the formation matrix, around the wellbore and into hydraulic fractures. Permeability reduction due to OIW and TSS are the result of complex physical mechanisms such as interception, bridging, sedimentation, straining, and attraction by surface forces (Farajzadeh 2004).

Reinjecting large amounts of produced water is likely to reduce the permeability and the corresponding injectivity around the injecting wellbore due to progressive formation damage, resulting in field operations to increase the bottom-hole pressure (BHP) to maintain injection rates. This BHP increase may eventually cause the creation of a hydraulic fracture, opening and propagating with respect to the in-situ stress field. Such fracturing will partially restore water injectivity and also change the pore pressure and stress field in the vicinity of the injector. With ongoing water injection, the formation damaging due to OIW and TSS continues in the presence of the hydraulic fracture. Over time, this can cause, again, a reduction in injectivity and together with in-situ stress changes multiple hydraulic fractures may be created, re-opened, and propagated until injection stops or equilibrium is reached.

For this field case study, the produced water reinjection may be implemented in the oil zone or in the surrounding aquifer. The unfavorable oil-water mobility ratio may require the injection of a polymer solution to improve the field recovery factor.

This results in four different scenarios to be investigated for the produced water reinjection (Fig. 1):

1. Water injection into the water leg
2. Water injection into the oil leg
3. Polymer injection into the oil leg
4. Conversion of a producing well into a water injector after a certain producing time.

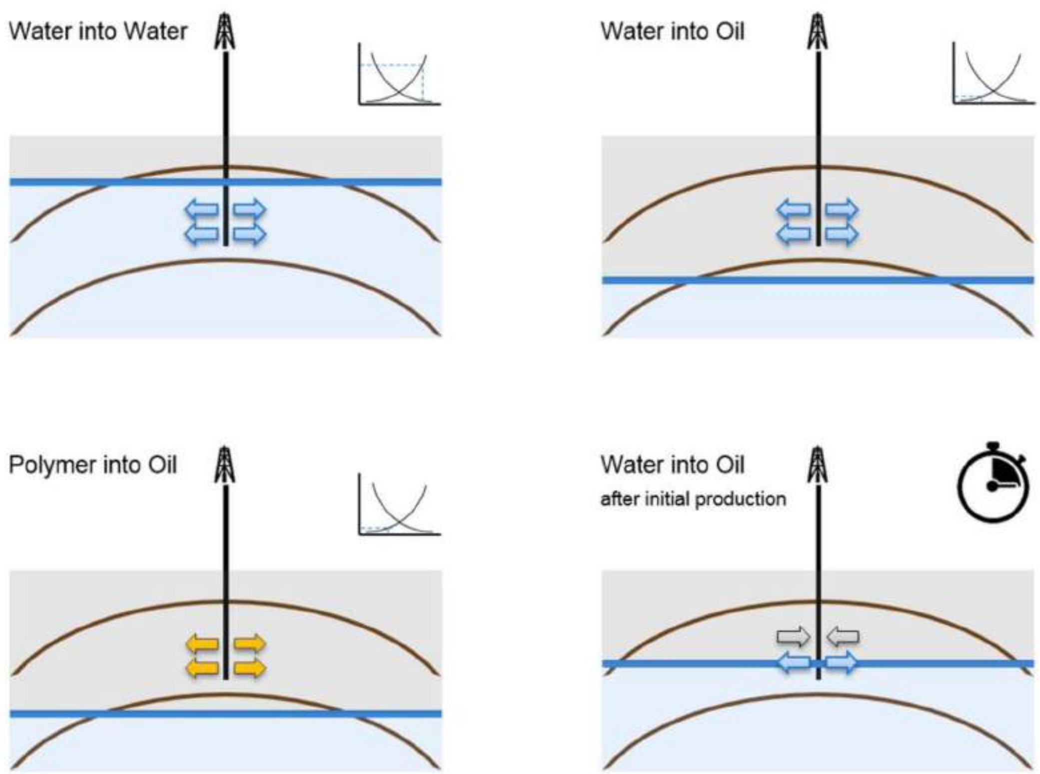

Figure 1—Summary of the four scenarios of produced water and polymer injection.

The predicted rapid pressure decline and offshore characteristics make produced water re-injection a key feature for reservoir management in this case study. Ideally, all produced water should be re-injected to maintain reservoir pressure. In practice, however, there are several risks associated with produced water reinjection that must be evaluated, such as the initiation of hydraulic fractures and their propagation into the cap rock, endangering reservoir integrity, or towards the water zone or a producing well, creating an undesired, highly permeable fluid flow path in the reservoir causing an early water breakthrough. Such phenomena associated with produced water reinjection are complex and the associated risks require an assessment that integrates the disciplines of reservoir simulation, formation damage, geomechanics, and hydraulic fracturing.

To the best of our knowledge, there is no end-to-end commercial solution to simultaneously model the formation damage due to injection of water impurities with reservoir flow, geomechanics and hydraulic fracturing. The aim of this study was to help close this gap by providing an innovative solution coupling the following specific models:

– Reservoir flow model accounting for multiphase flow
– Formation damage model predicting the permeability reduction, the corresponding well injectivity decline and BHP increase
– Geomechanical model computing the 3D stress changes associated to the pressure changes during fluid injection as changing due to fracturing
– Hydraulic fracturing model when the injection pressure is higher than the minimum in-situ stress, and a hydraulic fracture can be created and propagated

The workflow presented in this paper was designed within a research project to prove the concept and provide insights of a new degree of detail into the complex problem of hydraulic fracturing during produced water re-injection.

Proposed Methodology

The proposed workflow integrates multiple simulators in a single staggered coupling scheme (Fig. 2). During either the re-injection of produced water or polymer injection into the reservoir formation, the pressure build-up can result in the initiation of fractures around the well. The workflow includes an assessment of the likelihood of initiating hydraulic fractures under the given reservoir conditions and in case of generation the computation of the hydraulic fracture characteristics such as size and orientation, and an evaluation of the potential for propagation.

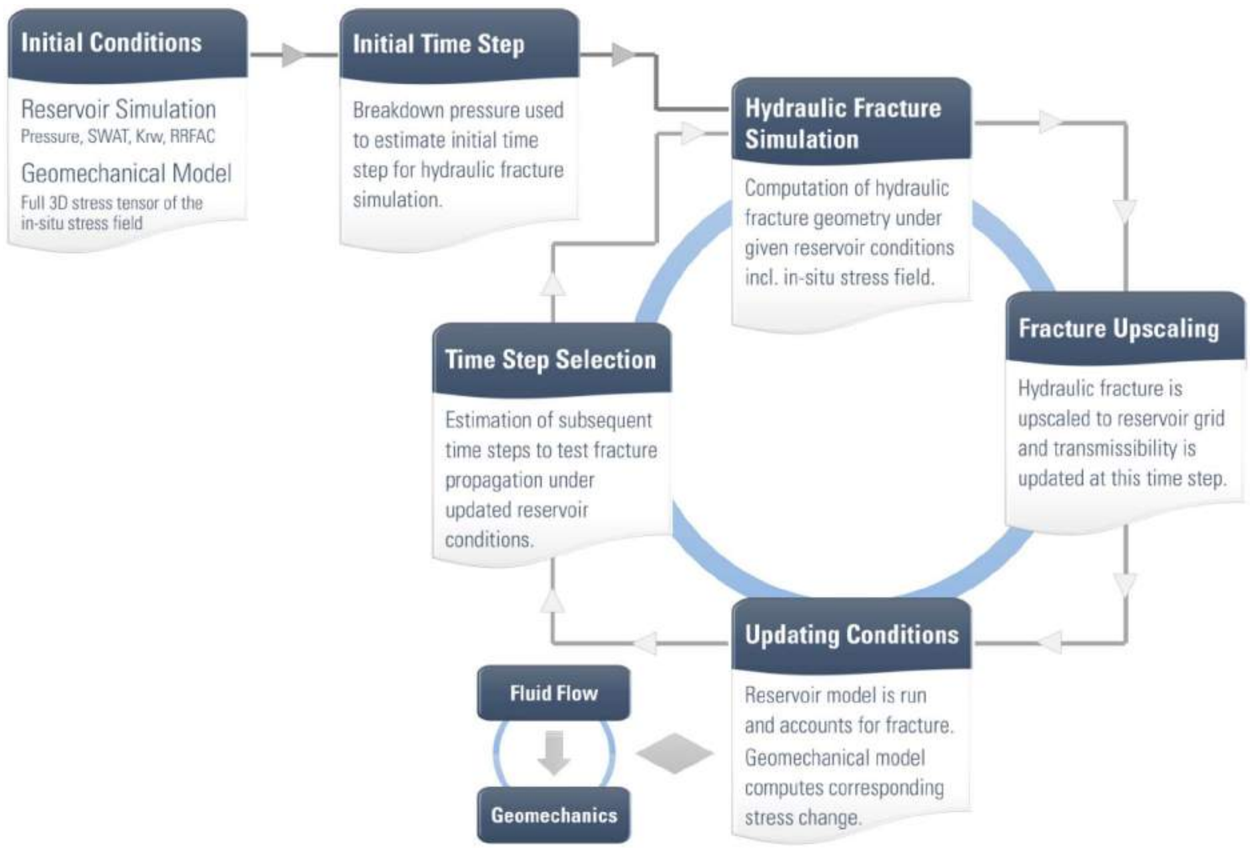

Figure 2—Outline of the integrated modeling scheme and workflow cycle.

Three simulators are coupled in the workflow to solve this problem: a fluid flow simulator (ECLIPSE) based on the numerical method of finite differences (FD) that was adapted to support the formation damage model, a geomechanical finite element (FE) simulator (VISAGE), and a hydraulic fracturing simulator (Kinetix Shale)[1].

The workflow is built around the hydraulic fracturing simulator, which is able to model the initiation and propagation of hydraulic fractures based on detailed descriptions of petrophysical and geomechanical properties, as well as the specific pumping schedule and fluid characteristics (e.g., Weng et al. 2014; Cohen et al. 2015). In particular, the built-in unconventional fracture model (UFM) is used due to its ability to consider the in-situ stress field and pre-existing hydraulic (or natural) fractures that can be re-opened and propagated further (Kresse et al. 2012). In addition to testing the conditions for initial fracture generation, the hydraulic fracturing simulator is thus able to provide complex fracture geometries and test the fracture propagation potential at various time steps during injection.

The fluid flow and geomechanical simulators with their respectively underlying reservoir model and geomechanical model, provide the conditions on which the hydraulic fracturing simulator is operating. To describe the in-situ pressure and stress conditions consistently, the reservoir simulation is directly coupled to the geomechanical simulation (e.g., Herwanger and Koutsabeloulis 2011; Mohamad Hussein et al. 2010; Zhang et al. 2011; Heffer et al. 2010).

Static properties provided to the hydraulic fracturing simulator include petrophysical parameters such as porosity and permeability, and rock mechanical parameters such as the Young's modulus and Poisson's ratio. Dynamic results include the reservoir pressure and water saturation from the reservoir simulation, and the in-situ stress field from the geomechanical simulation.

Fig. 2 outlines the main steps of the workflow. The first step focuses on the initial simulations performed by the fluid flow and geomechanical simulator, whose outcome describe the initial reservoir conditions. These simulations represent the main source of information for the following hydraulic fracture simulation.

In the second step of the workflow, the time step at which the hydraulic fracture simulation shall be run is defined. This time step definition is required by the staggered nature of the coupling workflow and is done by calculating breakdown pressures and comparing those to the BHP during injection. This gives an estimate of the time steps worth testing for fracture initiation by the hydraulic fracturing simulator. This calculation of breakdown pressure is done using an analytical solution assuming a penetrating fluid condition with a permeable borehole wall (Fjaer et al. 2008). Despite the assumption of a fully permeable borehole, the calculated breakdown pressure provides a conservative estimate of when hydraulic fractures are likely to be initiated, because plastic deformation and corresponding hardening are expected to retard the actual formation breakdown.

After the time step has been defined, all data describing the initial reservoir conditions are prepared for input into the hydraulic fracture simulation representing the third step of the workflow. The setup of the hydraulic fracture simulation includes multiple steps that can differ significantly depending on the type of input, reservoir characteristics and objective of the simulation.

The modeled injecting well is assumed to be open across the entire reservoir interval. The spatial domain for the simulation is given by a reservoir sector model, which is populated using the input data from the fluid flow and geomechanical simulation (Table 1).

Table 1—Summary of main input data provided from the fluid flow and geomechanical simulation to the hydraulic fracture simulation.

Parameters from fluid flow simulation	Parameters from geomechanical simulation
Reservoir pressure	Young's modulus
Porosity	Poisson ratio
Absolute permeability	Vertical stress
Gas/oil/water saturation	Maximum horizontal stress
Relative water permeability	Minimum horizontal stress
Residual resistance factor	Horizontal stress orientation

Since the formation saturation will govern the relative permeability of the injected fluid and different formation saturations as well as different viscosities of the injected fluid must be considered, special care must be taken in the description of the effective permeability experienced by the injection fluid. Instead of the total (absolute) permeability of the formation, the effective permeability that the injected fluid will experience is calculated considering the relative water permeability and permeability reduction due to modeled formation damage.

For the given field case conditions, the type of treatment fluid in the hydraulic fracture simulation is chosen to be water for three of the four scenarios, with the third scenario considering a water-based polymer fluid with 10 cP in situ viscosity. The pumping schedule was set up equal to the injection scenario of the reservoir flow simulation considering 6000 m^3/d or 4.16 m^3/min. The pumping time is defined by the total volume of fluid to be pumped, which typically varied between 100 and 500 m^3 (0.5 to 2 hours pumping time) depending on the scenario and time step. After fracture initiation, the injected fluid volume is successively increased during subsequent time steps to allow propagation.

Injecting increasing fluid volumes typically results in an increase in hydraulic fracture size. However, due to high permeability zones in the reservoir, fluid leak-off rapidly limits the growth of the hydraulic fracture and fluid efficiency drops significantly for increasing injection volumes and pumping times. The hydraulic fracture simulation finally provides the detailed fracture geometry as a simulation result (direction, height, length, and width).

To consider the presence of the generated fracture in the reservoir simulation, the converted hydraulic fracture is upscaled to the reservoir simulation grid in the fourth step of the workflow. An approximate fracture permeability is calculated based on the cubic law concept as a function of aperture. Using the Oda method (Dershowitz et al. 2000), the fracture permeability is upscaled to the grid cells hosting the fracture, resulting in an accordingly modified permeability field. Following the fracture upscaling, the fluid flow simulator is used to calculate a new transmissibility based on the updated permeability. Transmissibility multipliers are calculated to effectively reflect the generated hydraulic fracture.

In the fifth step of the workflow, the reservoir conditions are updated to account for the impact of the hydraulic fracture. The fluid flow simulation is re-run and modified dynamically, at the specific time step of fracture generation, using the generated transmissibility multipliers to account for the presence of the initiated fracture. In addition, the modified fluid flow simulation is coupled to the geomechanical simulation for obtaining the corresponding in-situ stresses at subsequent time steps.

After the reservoir conditions have been updated, the sixth step of the workflow closes the loop of the 'staggered' coupling scheme. It reflects the second step and aims at estimating the next point in time until the fluid flow and geomechanical simulation are run until a test for fracture propagation becomes suitable.

This starts the next cycle of the workflow and a new hydraulic fracture simulation is run while considering the updated reservoir conditions. These include updated information on pressure, saturations, and relative water permeability, as well as vertical and horizontal stresses. In addition, the initial fracture geometry is provided as pre-existing fracture to the simulation as subject to re-opening and propagation.

The described loop summarized in Fig. 2 is repeated until no further fracture initiation or propagation is computed and a stable solution is reached.

Modeling these processes by coupling different simulators requires a high-resolution geocellular grid to minimize any grid dependency of the results. This causes the computational costs to increase, since the required grid resolution is greater than the resolution of full-field reservoir simulations. To balance the need for high resolution with reasonable computation times, a sector model is built for the area of interest around the injecting wellbore selected for this study. Such a sector or submodel honors the structure of the encompassing full-field model and preserves fluid and rock properties. The sector model's horizontal dimensions were chosen to be twice the maximum expected length of any potentially created hydraulic fracture. Porosity, permeability, rock type, capillary pressure, and relative permeability, as well as rock mechanical properties, are provided by the full-field reservoir model. To properly simulate the average pore pressure increase around the wellbore due to the water injection, the sector model is surrounded by aquifers and their parameters are adjusted accordingly to match the average pore pressure history. The results of the hydraulic fracture simulation for the injecting wellbore can later serve as input to the full-field simulation to further adjust the history match and prepare the production forecasts.

Formation damage and the corresponding permeability reduction are modeled by internal features of the reservoir flow simulator. A macroscopic formation damage model is chosen, based on deep bed filtration and a few parameters, directly calibrated against laboratory measurements and field data, represented by Eq. 1 (Pang and Sharma 1994; Bedrikovetsky et al. 2001):

$$\frac{k_{red}}{k_{abs}} = \frac{1}{1+\beta C_{ads}} \tag{1}$$

where k_{red} designates the damaged (reduced) absolute permeability, k_{abs} the initial absolute permeability (i.e. before damage), C_{ads} is the concentration of the entrapped solid particles or adsorbed oil onto the rock surface, and β is the formation damage factor which has no dimension. C_{ads} may be obtained as a function of rock type and of C_{sol}, which is the suspended particle concentration in the mixture between the formation and the injected water, in a certain place in the reservoir, at a certain time.

The injected water contains solid particles and a non-negligible quantity of oil (OIW). According to Soo and Radke (1986), the transport of a dilute and stable emulsion is physically very similar to the deep bed filtration process. Therefore, the model described in this section for particle invasion in the formation remains unchanged for mixtures of particles and oil droplets. However, OIW may potentially increase the permeability reduction by TSS. Therefore, laboratory tests should be run in core plugs using injection water with the proper OIW and TSS concentration combination.

The fluid flow simulator applied in this study supports environmental tracers enabling the modeling of particle adsorption and desorption processes. However, calculating the resulting formation permeability reduction would require an additional external program. To streamline the proposed workflow and model formation damage entirely within the reservoir simulator, a "polymer" option was applied that allows the modeling of adsorption and desorption of polymer, which, in turn, allows the calculation of a relative permeability reduction factor, called residual resistance factor (RRF), as a function of the adsorbed polymer concentration.

To use this option, OIW and TSS total concentration replaces the polymer concentration and the viscosity multiplier of the polymer solution is set to one for all concentrations to preserve the original water viscosity. If polymer is added to the injected water, then the water viscosity multipliers, the adsorption curves, and the maximum residual resistance factor should be changed accordingly. The polymer model in the reservoir simulation software is represented by Eq. 2 and Eq. 3:

$$\frac{k_{rw\_orig}}{k_{rw\_maxads}} = RRF_{max} \tag{2}$$

$$\frac{k_{rw\_orig}}{k_{rw\_ads}} = 1 + (RRF_{max} - 1) * \frac{C_{ads}}{C_{maxads}} \tag{3}$$

In which k_{rw_ads} is the relative permeability of damaged zone, k_{rw_maxads} is the relative permeability of damaged zone at maximum adsorbed concentration (C_{maxads}), k_{rw_orig} is the initial relative permeability to water, with no damage, and RRF_{max} is the maximum residual resistance factor.

The relative permeability to oil k_{row_ads} is not affected by this model. This is a valid assumption if the rock is water-wet and the adsorption process is dominated by coating of the pore walls. On the other hand, pore-throat blocking may have a significant impact on oil relative permeability. Such limitation may not be significant due to the nature of the water reinjection and the corresponding high water saturation around the wellbore, where oil saturation should rapidly approach its residual value.

The polymer model and the Pang and Sharma (1994) model are equivalent for water flow.

If $k/k_0 \cong k_{rw_{ads}}/k_{rw_{orig}}$ then

$$\beta = \frac{RRF_{max} - 1}{C_{maxads}} \tag{4}$$

In the industry, laboratory tests are usually scarce or non-existent. Therefore, the permeability reduction model must be calibrated through a history match of the injection well behavior. However, such a history match must be bounded by physical limits of the adsorption curves and residual resistance factor. We derived simple equations to estimate such bounds, considering two entrapment/adsorption models: coating the pore walls and blocking the pore throats.

Fig. 3 presents a diagram illustrating the injection-dilution-adsorption-permeability reduction process. As the produced water containing OIW and TSS particles is injected, it is partially diluted in the formation water. According to the resulting concentration of OIW and TSS in the region near the wellbore, a fraction of the particles is adsorbed or entrapped by the rock. The fraction of the particles that is not adsorbed will be suspended in a more diluted suspension, which will move forward and away from the wellbore. Such adsorption process continues until there are no more suspended particles.

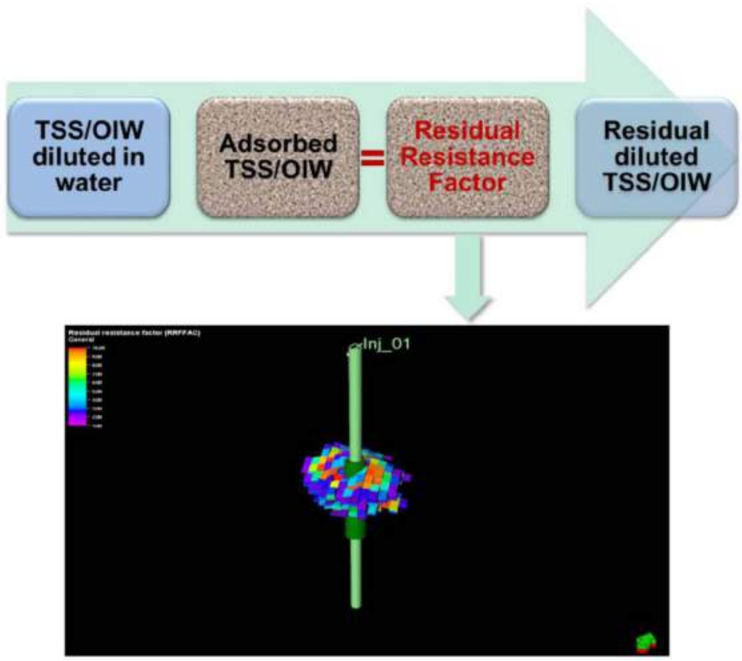

Figure 3—Outline of the OIW and TSS material balance and volume of rock affected by the resulting RRF, i.e. a permeability reduction.

With time, the adsorbed and entrapped fractions may locally reach a maximum over which any OIW and TSS injected directly pass through, moving forward and away from the wellbore. As time goes by, an increasing volume around the wellbore is contacted by the OIW and TSS suspension. Because of the radial nature of such affected rock volume, it tends to grow slower and slower. The RRF increases to a maximum according to the adsorbed concentration of OIW and TSS. Naturally, the highly permeable rock regions around the wellbore will receive most of the injected water, will thus absorb most of the OIW and TSS, and will consequently show the highest values of RRF (Fig. 3).

Fig. 4 illustrates the concept of injection well history match while considering the described damage modeling. The blue curve shows the observed injectivity index history. The red curve is the result of the history match between such an injectivity history and the injectivity estimated by the model for permeability reduction due to formation damage.

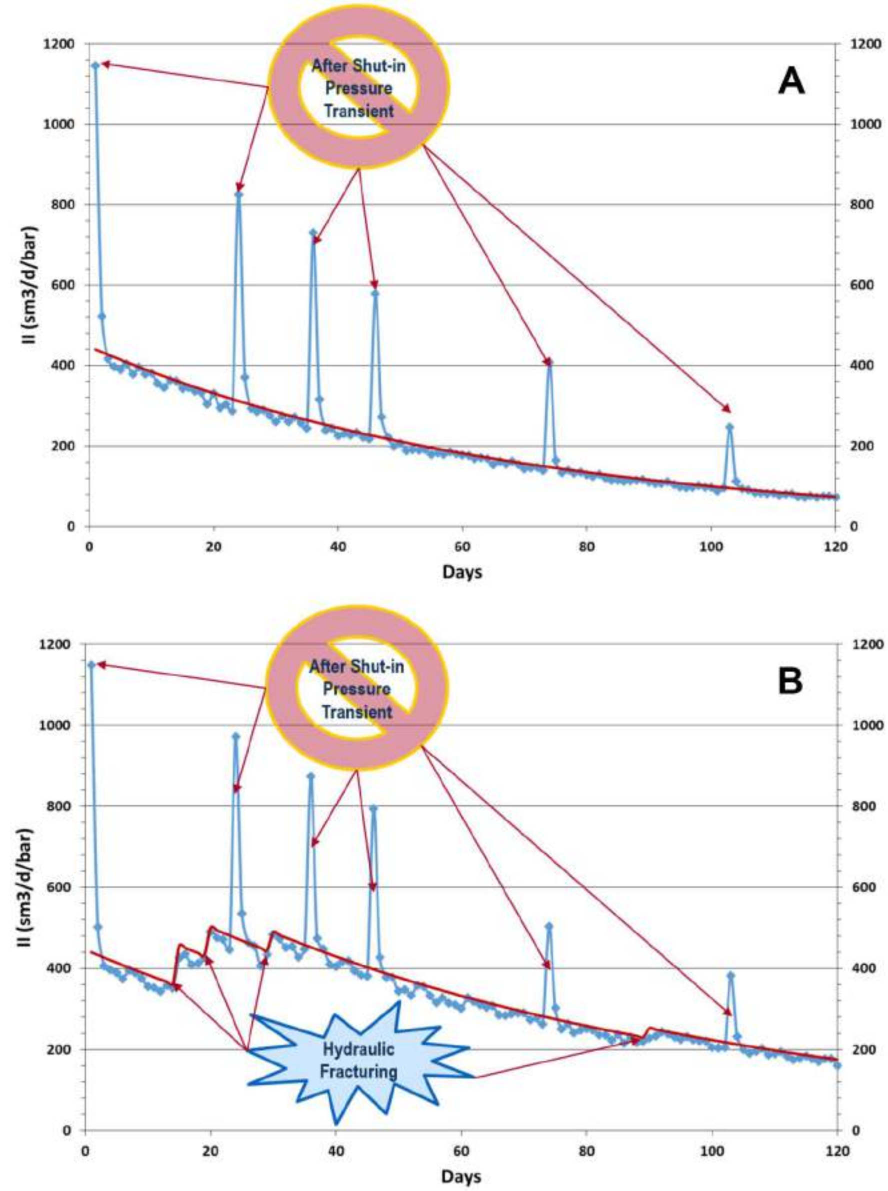

Figure 4—Example of a well injectivity history match model, without (A) and with (B) hydraulic fractures being considered.

The maximum RRF and the adsorption curves are adjusted to perform the history match. The maximum RRF moves the estimated injectivity curve up and down, and the adsorption curves change the shape of the injectivity curve.

In Fig. 4A, hydraulic fractures are not considered. It is important to be aware that local injectivity increase right after a well shut-in period should not be mistaken as hydraulic fracture indication. It is a pressure transient behavior and its duration may be estimated from the average well permeability and fluid properties. If time steps and rates are refined during the flow simulation, such a transient behavior should be matched by the estimated injectivity curve. Fig. 4B shows the history match process considering the hydraulic fractures and the resulting local increase in injectivity. If the temperature of the injected fluid differs significantly from reservoir temperature, thermal calculations must be considered by the fluid flow simulation as well.

In addition to the domain of fluid flow, the geomechanical characterization of the field and reservoir rock is key for modeling hydraulic fracture development. The proposed workflow applies the Mechanical Earth Model (MEM) concept, which is an internally consistent representation of the state of stress, pore pressure, and rock mechanical properties for a specific section in the subsurface. Fig. 5 shows a schematic representation of a MEM setup including the geological and structural framework, the mechanical stratigraphy, and the corresponding stress profiles.

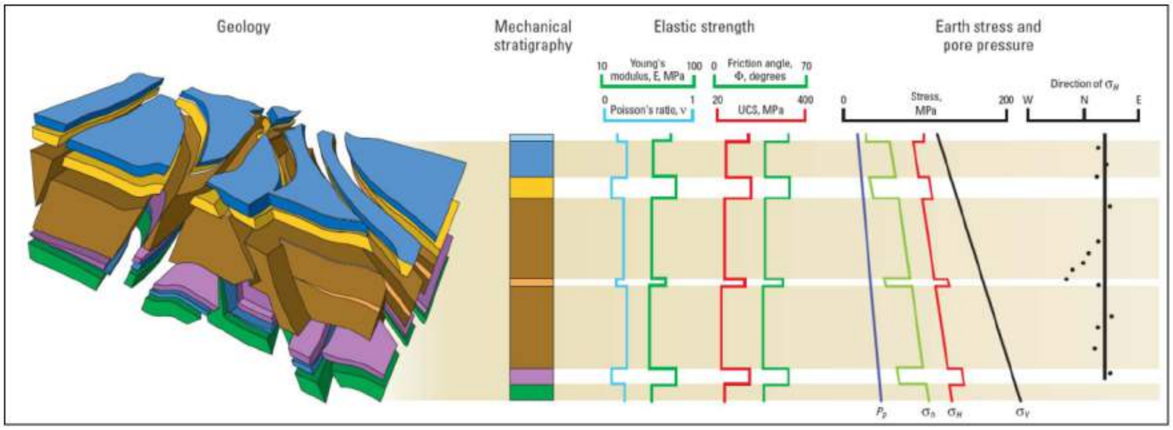

Figure 5—Concept of the Mechanical Earth Model (after Ali et al. 2003).

For the construction of the MEM, a multidisciplinary workflow is required including the domains of geology, log analysis, rock physics, laboratorial test interpretation, drilling, and reservoir engineering. A rigorous methodology is adopted, including exhaustive calibration, aiming to represent all geomechanical phenomena observed in the oil field. Literature is vast on the matter and some examples are found in Plumb et al. (2004) and Frydman and Ramirez (2006).

The MEM can be developed in 1D or in 3D, depending on the objectives and information available. 3D MEMs can be coupled to reservoir simulations for time-lapse insights into the stress field beyond the initial state of stress. For the proposed method, a 3D MEM is required due the intrinsic nature of the problem. The workflow for 3D MEM building and a description of methodologies and examples are discussed on Herwanger and Koutsabeloulis (2011).

Case Study

Following the setup of a full-field fluid flow simulation for the entire reservoir, a sector model was built surrounding a selected injecting well. This sector grid comprises 320,000 active cells in total with a resolution of 50 m × 50 m in the horizontal direction and thickness ranging from 0.16 m to 3.14 m.

The sector model preserved the fluid and rock properties of the underlying full-field model in the selected area. Oil and water properties, porosity, permeability, rock type distributions, mechanical properties, and relative permeability curves were identical to those of the parent model. Although the selected well is a deviated well, a simplified, vertical well trajectory was chosen for this proof of concept study to make it easier to quality control the results of the integrated workflow. To properly simulate the pore pressure increase forecasted by the full-field model, the sector model was surrounded by aquifers, and their parameters were adjusted accordingly (Fig. 6).

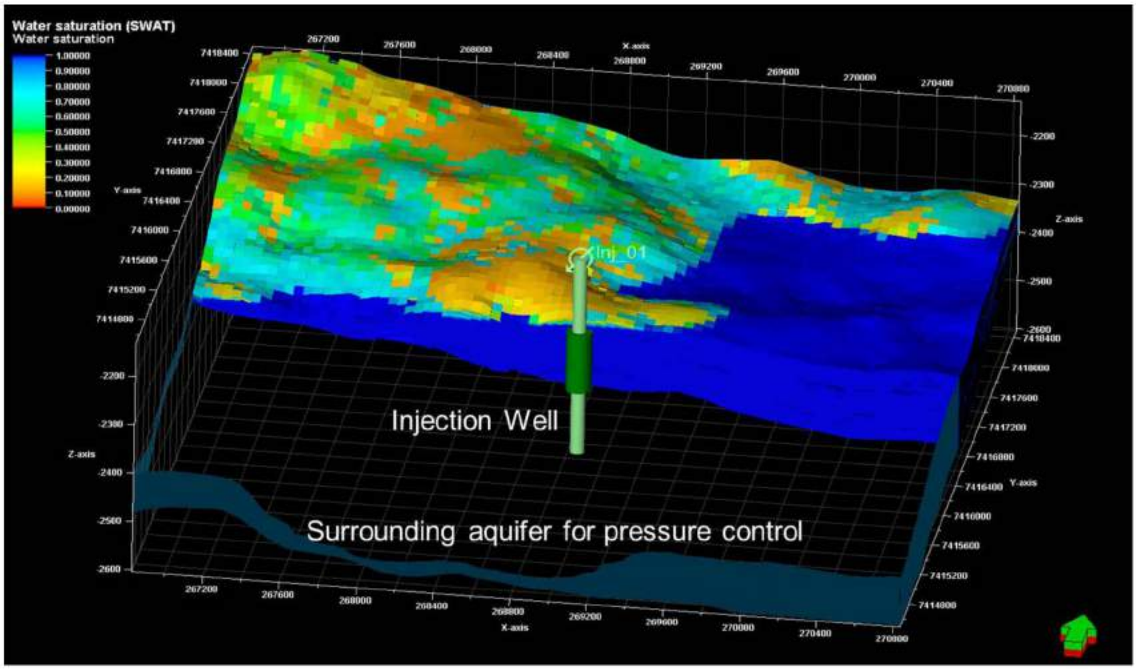

Figure 6—Reservoir sector model around the injection well showing initial water saturation and the aquifer definition at the border of the modeled area.

The reservoir sector grid was considered suitable to model the BHP and near wellbore pore pressure buildup for the purposes of the developed workflow. Within the sector grid generation, tests using a locally refined grid around the injector showed that the changes in BHP and pore pressure near the wellbore were minor. Therefore, the chosen grid already comprised sufficient resolution.

The surface temperature of the reinjected produced water is very close to the reservoir original temperature and the subsea temperature drop is small. Therefore, the temperature effects were not significant for this particular case.

A 3D MEM was built for the entire field. This included the build-up of the structural model, compilation and QC of all log data, and an analysis of 16 wells regarding wellbore stability to achieve a consistent geomechanical calibration of the field.

An extensive dataset of multi-cycle extended leak-off tests was available and was analyzed for minimum in-situ stress calibration points. Moreover, a comprehensive dataset of rock mechanical laboratory test results was available, including triaxial test results, pore volume compressibility tests, and hydrostatic compaction tests. This data were analyzed and used to define the constitutive model for the reservoir rock. Beyond poro-elastic behavior, the modified Drucker-Prager criterion was chosen as appropriate yield criterion.

The original reservoir grid was embedded into its surrounding rock mass by adding an extended grid for overburden, underburden, and sideburden. The embedding is used to minimize effects of boundary conditions on the area of interest. Following the grid generation, geostatistical methods were used to populate the rock properties using upscaled well data, seismic velocities, and related properties (porosity and facies) from the pre-characterized reservoir. The mechanical behavior of faults was modeled using the equivalent material concept, in which normal and shear fault stiffness are considered in combination with the elastic behavior of the intact rock mass (see, e.g., Pande et al. 1990; Koutsabeloulis and Rylance 1992). For the pore pressure definition describing pre-production conditions, the active cells of the reservoir were populated with the original pressures of the reservoir model. For the other cells, pore pressures were assigned according to the single well analysis, assuming constant pressure gradients in the formations. The finite element method (FEM) was used to compute the stress equilibrium of the 3D geomechanical model.

Subsequently, the optimal set of boundary conditions was iteratively optimized to match the single-well stress models and closure pressures from field measurements.

To accelerate the simulations of the workflow cycle, the previously generated sector model was also considered for the geomechanical simulation in the proposed workflow. Fig. 7 shows the full reservoir and identifies the size and location of the modeled sector. Similarly to the full-field 3D MEM, the sector model was also embedded to consider a sideburden, overburden, and underburden, as shown in Fig. 8, and includes 1.34 million elements in total.

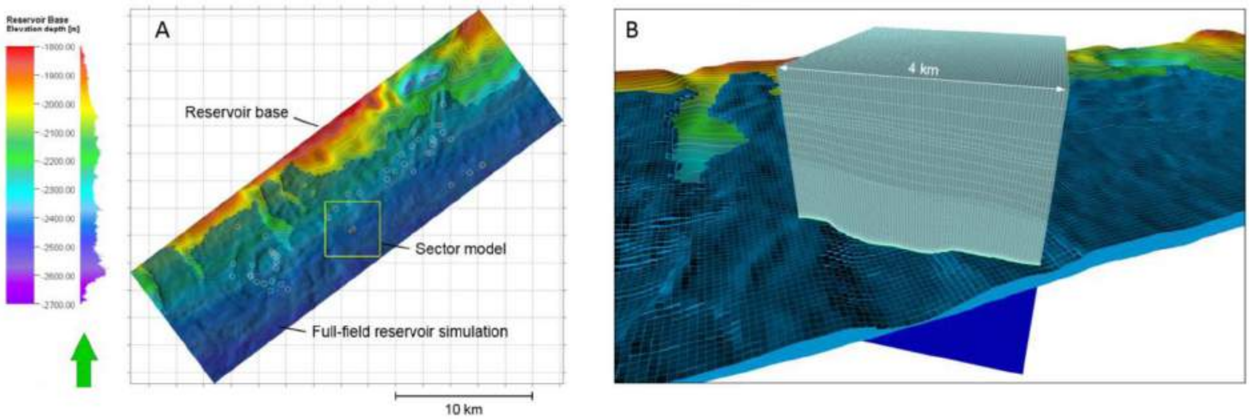

Figure 7—A) Top view on the reservoir showing the reservoir base in the background and outlining the sector model size and location. B) Side view on the sector model showing its resolution in context of the full-field reservoir simulation grid.

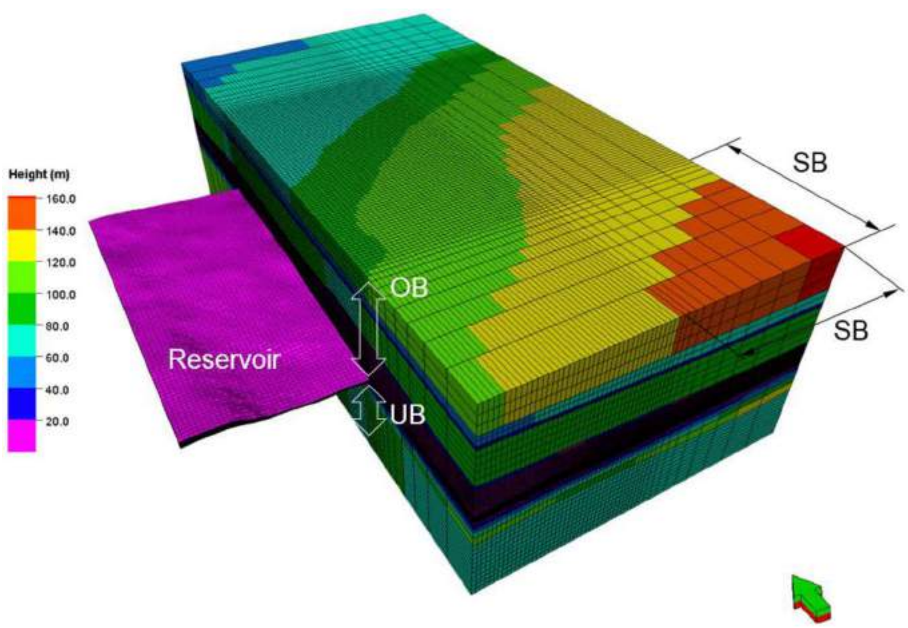

Figure 8—Overview of the geomechanical grid of the sector model showing the cell thickness distribution in the reservoir part and in the overburden (OB), underburden (UB), and sideburden (SB).

The sector model was populated with mechanical properties provided by a well placed in this area, and the properties were laterally propagated. The same approach was used for the pore pressure gradient. Due to the lack of significant plasticity in the full-field model for the sector model area, the reservoir rock was assumed to behave linear elastic within the sector model. A stress/strain simulation was conducted using the following boundary conditions: 1) base of the grid was constrained in the vertical direction; 2) strains were imposed at the lateral boundaries; 3) a sea fluid surcharge was applied on top of the model. A 1D MEM was available for the primary source well in this sector and was used to check for a good match of the computed stresses and mechanical properties between the 1D and 3D model.

Fig. 9 shows the in-situ 3D stress field in terms of principal total stress magnitudes in the sector model. This state of stress represents the starting conditions for the proposed workflow. In particular, the distribution of the third principal stress, which represents the minimum horizontal stress under the prevailing normal faulting regime, shows the impact of the mechanical stratigraphy on the stress profile.

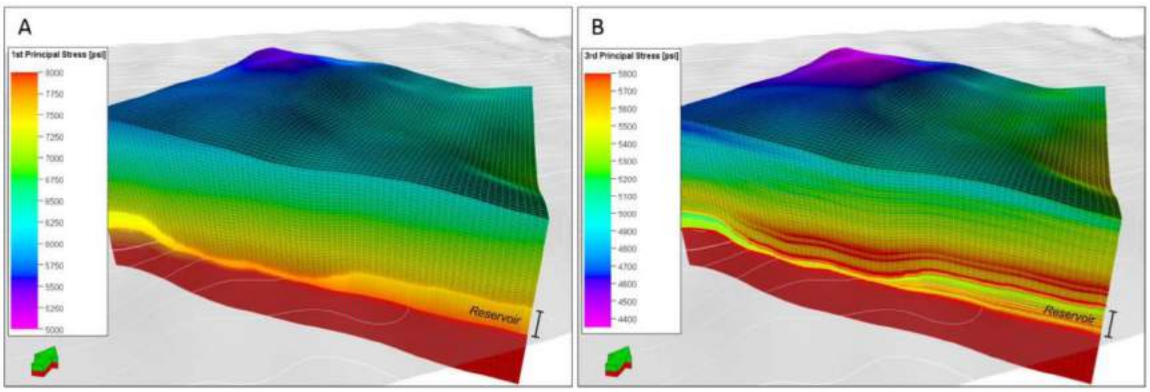

Figure 9—3D distribution of the first (A) and third principal (B) total stress magnitudes in the reservoir and adjacent zones of the sector model.

The polymer option keywords used in the fluid flow simulation are summarized in Table 2. Their columns and corresponding values were obtained modeling the entrapment of OIW and TSS by the rock, since there were no laboratory data for permeability reduction due to formation damage.

Table 2—Polymer option keywords and values used in the fluid flow simulator.

Keyword	Column	Unit	Values				
POLYMER							
PLYMAX	Maximum C_{sol}	Kg/sm³	0.04				
	Salt Concentration	Kg/sm³	0.00				
PLMIXPAR	Todd-Longstaff param.	-	1				
PLYROCK	Dead pore space	-	0.00				
	Maximum RFF	-	10.0				
	Rock density	Kg/rm³	2500				
	Adsorption index	-	2				
	Maximum C_{ads}	Kg/Kg	0.0001				
PLYVISC	C_{sol} array	Kg/sm³	0.00	0.01	0.02	0.03	0.04
	μ_w multiplier array	-	1	1	1	1	1
PLYADS	C_{sol} array	Kg/sm³	0.00	0.01	0.02	0.03	0.04
	C_{ads} array	Kg/Kg	0.0000	0.00004	0.00008	0.00009	0.0001

Maximum C_{sol} corresponds to an average of 0.04 kg/sm3 of OIW and TSS in the produced water. A simple pore-throat-blocking model was applied to the main reservoir rock type, based on average porosity, and average pore-body and pore-throat sizes, to estimate a maximum C_{ads} of 0.0001 kg/kg. We set the maximum residual resistance factor to 10 as the result of a preliminary history match of the selected well.

Results

Permeability Reduction History Matching

For the first scenario, reflecting injection into a water-saturated zone, a good preliminary history match of the damage model could be achieved for the selected injection well. Field data to do such a history match were only available for this scenario. Short-term pressure transients were not considered due to constraints on data availability and grid refinement. Fig. 10 shows a summary of the observed and simulated injectivity and BHP. This history match allowed the definition of the maximum RRF and the initial adsorption curves were considered correspondingly.

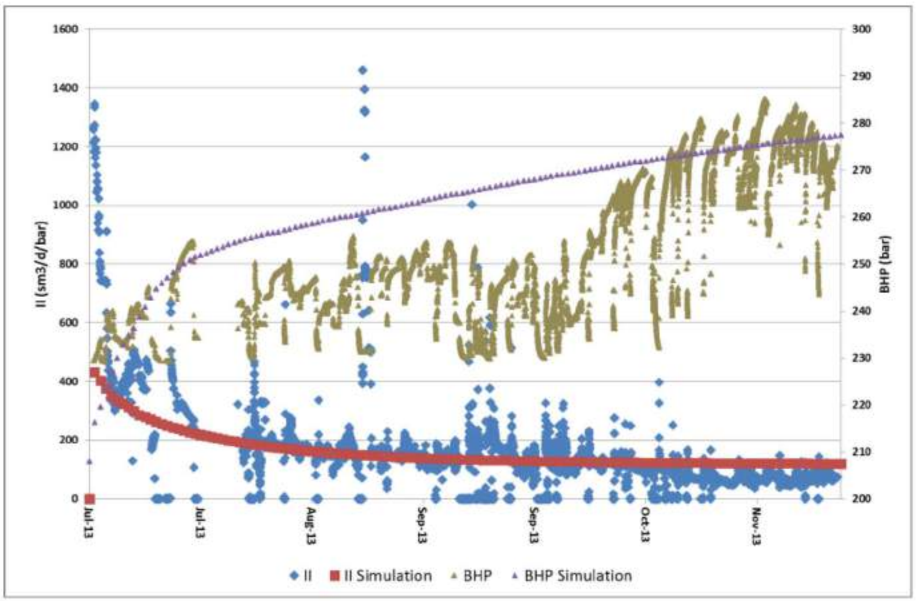

Figure 10—Comparison between the observed well injectivity history (blue) and simulation results (red), with correspondingly observed (gold) and simulated injection BHP (purple) in the water-leg scenario.

Fig. 11 shows the RRF distribution around the wellbore, and the corresponding volume affected by permeability reduction, resulting from adsorbed OIW/TSS concentration after a 10-year period of produced water reinjection in the water saturated region without considering any hydraulic fracture development. The average radius of the affected region was 150 m with a maximum RRF of 10.

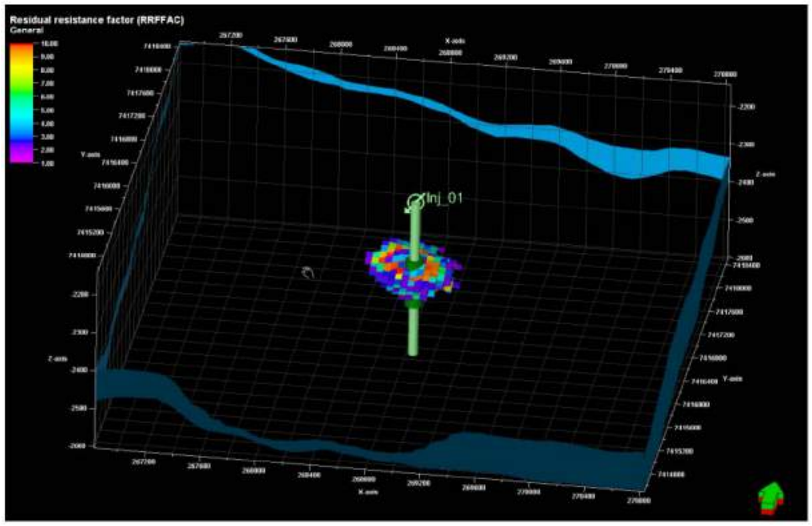

Figure 11—Volume around the wellbore affected by permeability reduction computed by the damage model showing the RRF after 10 years.

Fig. 12 compares the well injectivity index with and without impairment from OIW/TSS impurities, in the water-leg scenario. In the first 2 months, the injectivity index was reduced from 420 to 140 sm3/d/bar. After 6 months, the well injectivity index reached a stable value of 120 sm3/d/bar, approximately three times less than the value of 350 sm3/d/bar when no permeability reduction was considered.

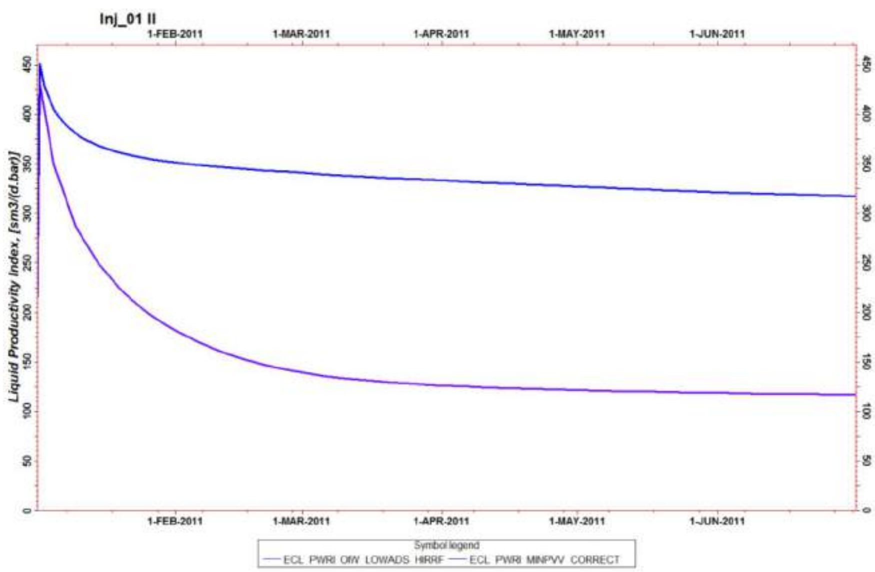

Figure 12—Comparison of well injectivity index without (blue) and with (purple) permeability impairment from OIW/TSS impurities, in the water-leg scenario.

During the injection of produced water in a well completed in the oil leg, oil and water saturation around the wellbore need to be considered changing with time. Initially, the water saturation is nearly irreducible, and relative permeability to water is negligible. Therefore, initial well injectivity is very low. Ramping up water injection is usually used to prevent immediately inducing fractures. As water is injected, water saturation around the wellbore increases, which increases well injectivity. However, because produced water with impurities is injected, the permeability around the wellbore is reduced. Fig. 13 shows such behavior, comparing the base case (blue) with the permeability reduction case (green), for which the injectivity change was significantly less pronounced but still increasing with time. At the end of simulation period, the injectivity index was 220 sm3/d/bar for the base case and 80 sm3/d/bar for the OIW/TSS case.

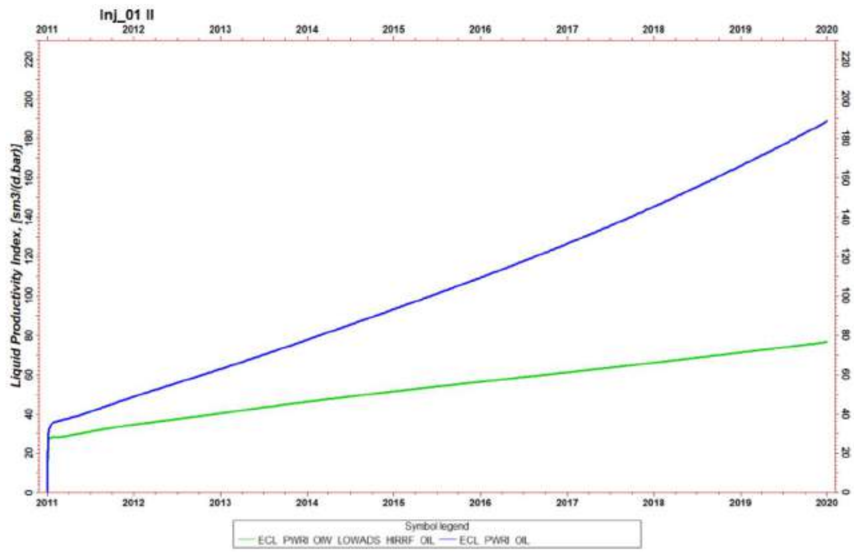

Figure 13—Development of the well injectivity index for the oil-leg scenario without (blue) and with (green) permeability impairment from OIW/TSS impurities.

The changes in water saturation, relative permeability, and behavior of the residual resistance factor in the oil-leg scenario are presented in Fig. 14. For a specific cell close to the wellbore, the RRF, water saturation, and water relative permeability are compared between the base case and the case with permeability reduction (i.e., the damage model being considered). RRF increases to its maximum value within a year. Water saturation slowly increases with the corresponding increase of the relative permeability to water. In this particular cell, the water saturation increases faster when permeability reduction is considered.

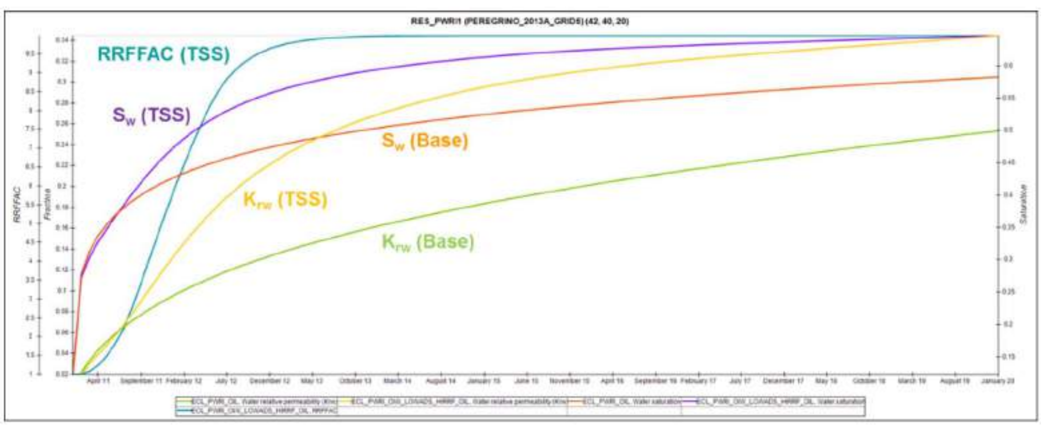

Figure 14—RRF, water saturation, and relative permeability development over time in the oil-leg scenario, for a single cell close to the wellbore.

In the hydraulic fracture simulation, the effective permeability for the injected fluid is considered as changing with formation saturation. Fig. 15 shows the water relative permeability distribution after 10 years of injection.

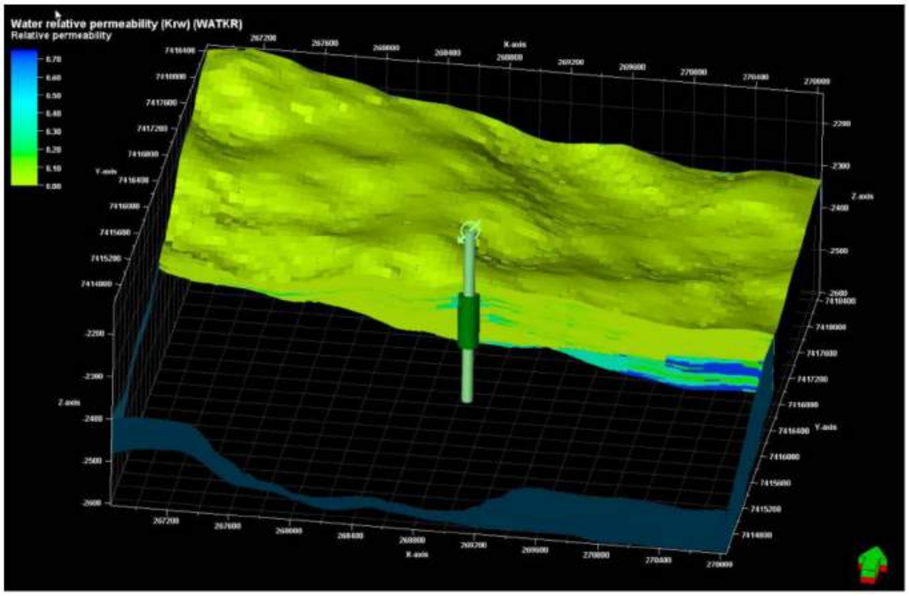

Figure 15—Water relative permeability in the sector model after 10 years of injection.

The flow simulation results showed significant impact of formation damage and initial saturation conditions in the reduction of well injectivity to produced water and the correspondent increase of BHP. Therefore, these conditions are considered for the simulation hydraulic fracture development in the four scenarios.

Hydraulic Fracture Development

The outlined workflow (Fig. 2) was sequentially applied to the four scenarios (Fig. 1) differing in the assumed formation saturation, injection fluid viscosity and timing. The results summarized below showed new insights into the hydraulic fracture development during produced water reinjection into a conventional reservoir.

Scenario 1: Water injection into water leg. In the first injection scenario, the formation was assumed to be water-saturated. The fluid flow model showed a steady increase of the BHP over time, which was stronger in the first 4 months and then declined. Over the first 3 years, the BHP remained significantly below the minimum breakdown pressure. This observation also did not change when considering an amplification of the damage model (i.e., by increasing the permeability reduction due to chemical adsorption and particle filtration). In addition, the applied breakdown calculation yields generally more conservative values, and the breakdown pressure will further increase with pressure and total stress.

This observation suggests that the initiation of a hydraulic fracture was unlikely in this scenario, and this was confirmed by the hydraulic fracture simulator, which was unable to initiate any fracture. This scenario also underscored the importance of the effective permeability experienced by the injected fluid, which appeared in this scenario to be high enough to prevent the net pressure build-up from initiating a hydraulic fracture. The simulated formation damage also did not yield a decrease in permeability sufficient to change that and counteract the increase of the breakdown limit due to increasing pressure and total stress.

Scenario 2: Water injection into oil leg. The second scenario considered water injection into an oil-saturated formation. Due to the much smaller water relative permeability around the wellbore, this yielded a significantly stronger increase in BHP than in the first scenario.

At the selected time step, reservoir conditions were provided by the fluid flow and geomechanical simulation. Two bands of high permeability at the well were also the areas of most significant increase in reservoir pressure due to preferred influx. This pressure increase was accompanied by a corresponding increase in total stress. Fig. 16 shows the hydraulic fracture simulation results for the first time step in this second scenario, which suggest the initiation of a considerable hydraulic fracture propagating symmetrically from the well.

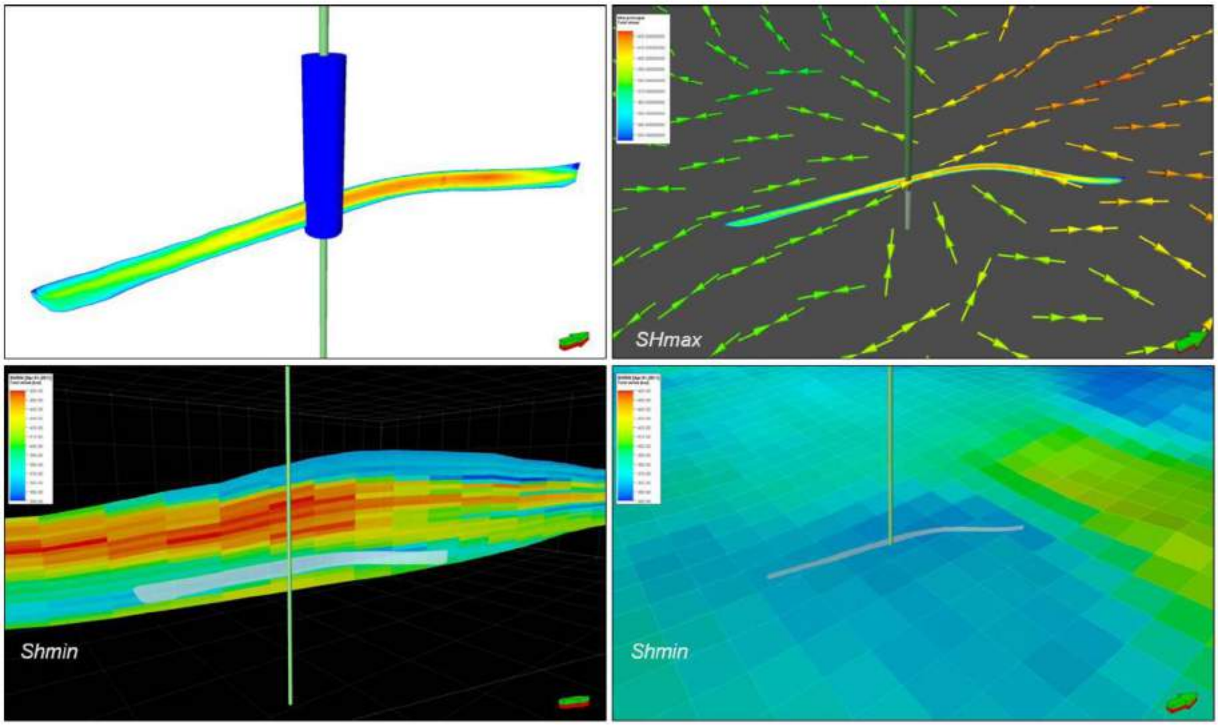

Figure 16—Initial hydraulic fracture of oil-leg scenario shown with contours of fracture width (top left), and plotted against SHmax trajectories (top right) and Shmin magnitude on a horizontal cross section (bottom right), as well as in front of a vertical cross section showing Shmin magnitude (bottom left).

This fracture was likely to have a length of up to 330 m with a height of about 16 m. It followed the in-situ maximum horizontal stress direction and was initiated in the lower part of the reservoir (Fig. 16). In this interval, the effective permeability was low, which limited the leak-off and allowed the build-up of net pressure for fracture initiation. The low total minimum horizontal stress additionally provided less resistance to fracture opening and propagation. Surrounding zones of higher stress and permeability seemed to spatially limit the fracture.

The hydraulic fracture was upscaled to the reservoir grid and used to update the permeability field as outlined above. The fluid flow simulation was modified to account for the hydraulic fracture at the time of its generation. Fig. 17 compares the pressure profile during injection in the unmodified and modified fluid flow simulation case at the depth level of the fracture. Although the fracture influenced the pressure profile, its impact appears to be local. The overall pressure distribution did not change significantly, especially at some distance from the well, which underlines the importance and primary control of the original permeability distribution.

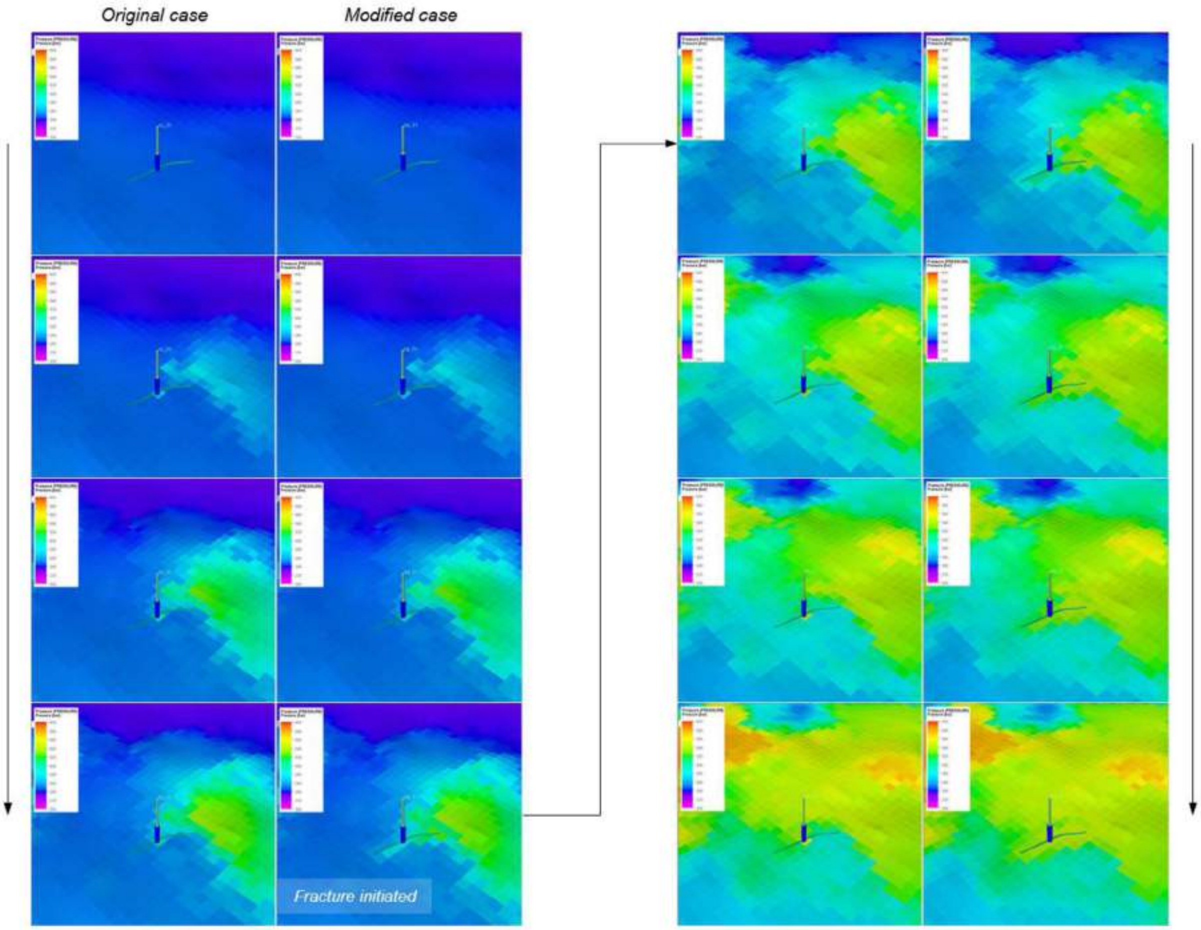

Figure 17—Pressure profile over time without and with accounting for the generated hydraulic fracture in the oil-leg scenario. Please note that the fracture is always shown for reference, but its impact is only included in the modified case after the marked time step.

Following the initiation of the hydraulic fracture, its potential to propagate was evaluated. Fig. 18 shows the development of reservoir pressure at the well for the unmodified and modified fluid flow simulation. The emplacement of the hydraulic fracture caused the pressure to drop, which was accompanied by a corresponding decrease in total stress. These conditions were thus most favorable for fracture propagation.

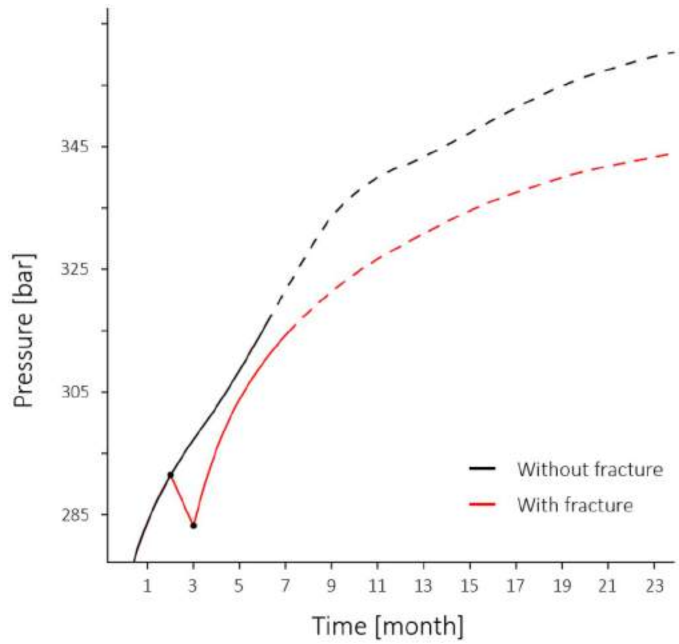

Figure 18—Impact of the initial hydraulic fracture generation on the pressure profile at the injecting well.

Updated reservoir conditions, as well as the geometry of the initial hydraulic fracture, were provided as input to the hydraulic fracture simulation for the following time step. Four time steps reflecting four iterations through the workflow cycle were required and performed in this scenario until a final, stable solution was found (Fig. 19).

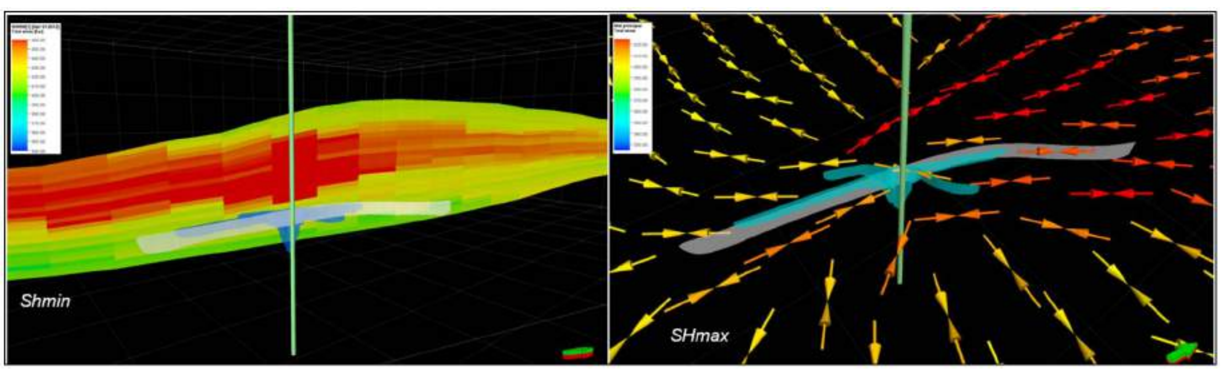

Figure 19—Hydraulic fracture simulation result at the fourth time step (i.e. fourth iteration of the workflow cycle) shown in context of a vertical cross section of Shmin magnitudes (top left) and with SHmax trajectories underlining the alignment of the fracture with the stress field. The results show partial re opening of the initial fracture (white) and initiation of additional fractures of minor size.

The hydraulic fracture was re-opened and propagated by about 50 m during the following time steps before it was only partially re-opened and propagation ceased. In the final time step, minor fractures were newly initiated, which were following the significantly rotated in-situ stress field (Fig. 19). The height growth potential of the fracture appeared to be very minimal. Especially upward propagation was limited due to pressure increase in the high permeability zones above the fracture, which resulted in a pronounced stress barrier.

The results of this second scenario suggest that the initially created fracture steered the following development, whereas the in-situ stress state and its changes drove the re-opening and propagation behavior. Eventually the fracture development stabilized and became a near-well phenomenon.

Scenario 3: Polymer injection into oil leg. The third scenario considered the injection of a polymer into an oil-saturated formation. This scenario was similar to the previous oil-leg scenario, but with the exception of a significant increase in viscosity of the injected fluid. The higher fluid viscosity yielded a considerably stronger increase in BHP with time, and therefore the time steps for the workflow were reduced.

Reservoir conditions for the first time step showed a more localized increase in reservoir pressure and total stress around the well, which can be attributed to the higher viscosity of the injected fluid over the shorter injection time of several days.

The results of the hydraulic fracture simulation showed the initiation of a significantly asymmetric fracture (Fig. 20). As in the previous scenario, the fracture was generated in the low permeability section of the reservoir and had a similar total length of about 310 m. However, the fracture height of about 30 m was significantly larger when injecting polymer. The results showed that the fracture is aligned with the maximum horizontal stress and its asymmetric behavior is also caused by the in-situ stress field driving the fracture propagation towards lower stress regions.

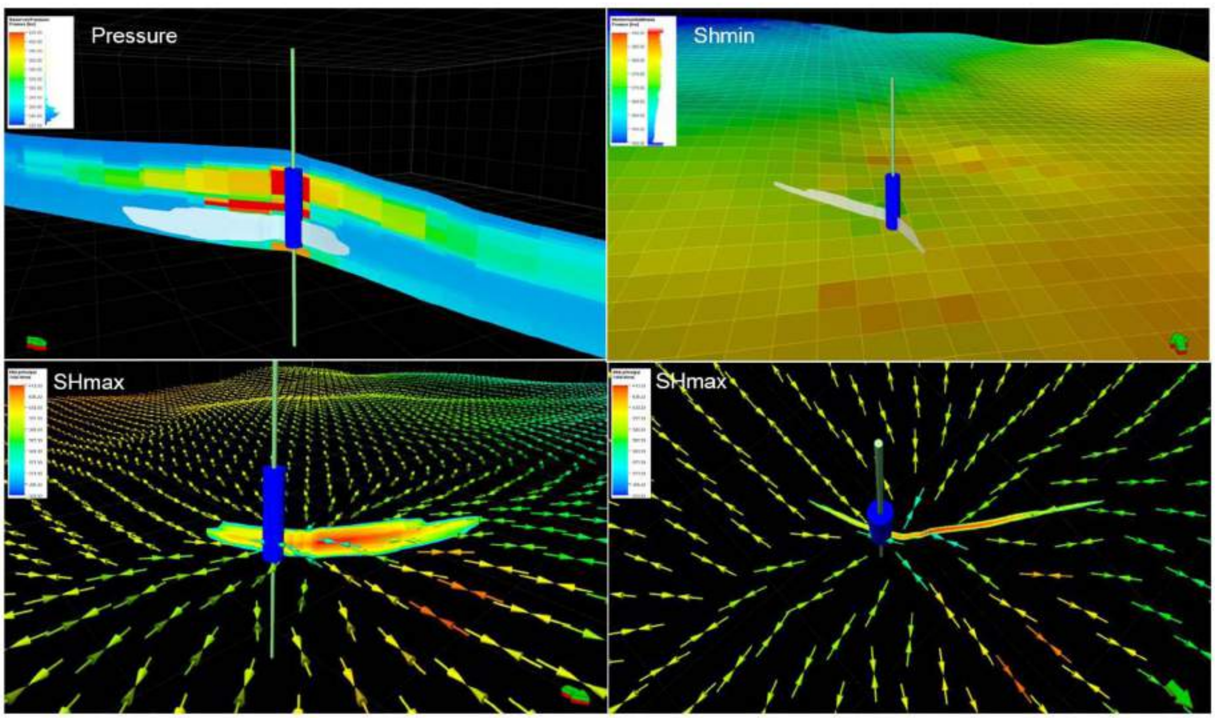

Figure 20—Asymmetric initial hydraulic fracture in the polymer scenario shown in context with the vertical reservoir pressure profile (top left) and the lateral distribution of Shmin magnitudes (top right). The fracture contoured with aperture is also plotted against SHmax trajectories (bottom).

After upscaling the fracture to the reservoir grid and updating the permeability field, the fluid flow simulation was able to account for the hydraulic fracture at the time of its generation. Fig. 21 compares the pressure profile of the unmodified and modified simulation during polymer injection at the depth level of the fracture.

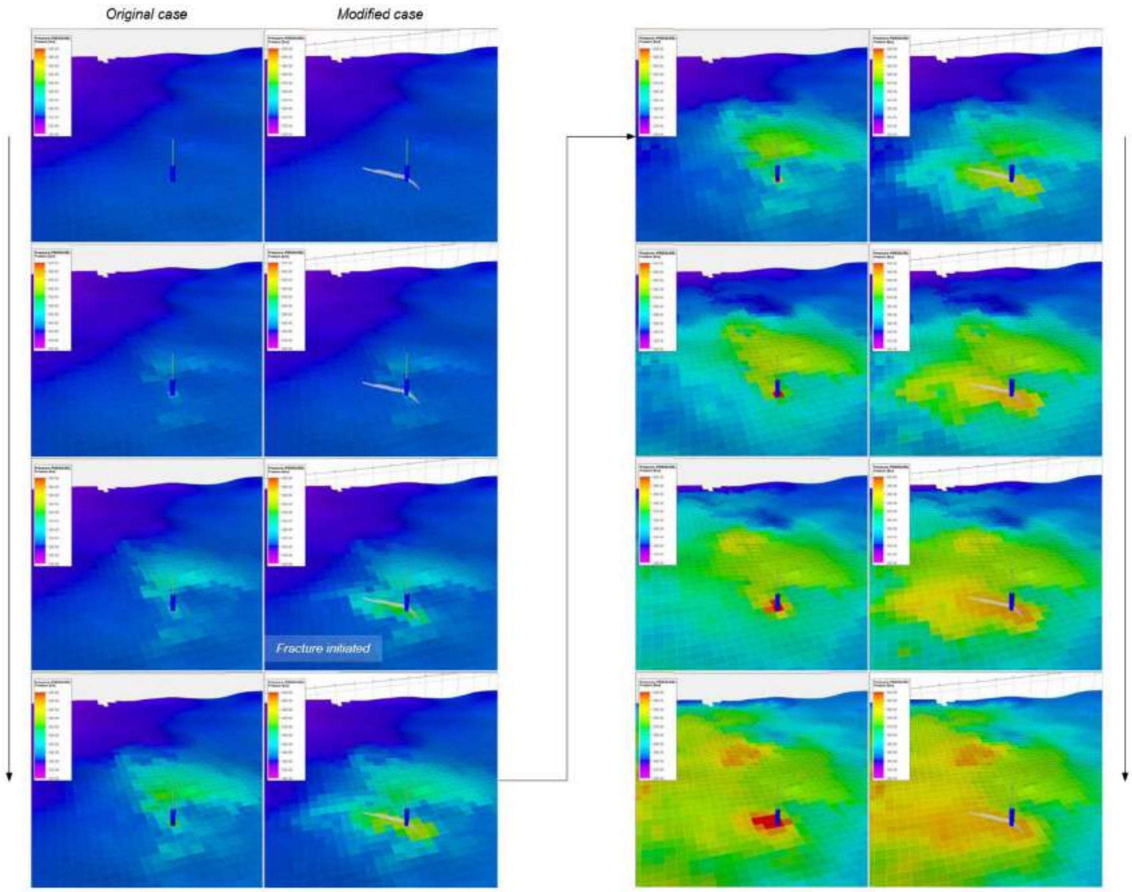

Figure 21—Pressure profile over time without and with accounting for the generated hydraulic fracture in the polymer scenario. Note that the fracture is only included in the modified case after the marked time step.

After fracture initiation, the enhancement of fluid flow yielded a more widespread increase in pressure (Fig. 21). With ongoing injection, the fracture dissipated pressure and prevented a local pressure build up around the well. Although the impact of the hydraulic fracture appeared stronger in this scenario than in the previous one, it had still a rather local impact compared to the reservoir size.

In the following time steps and workflow cycles, the simulation results showed a significantly asymmetric fracture propagation in total of about 200 m that yielded an overall more symmetric fracture geometry (Fig. 22). It is presumably the asymmetric geometry of the initial fracture and the correspondingly asymmetric enhancement of flow and build-up in pressure and stress that drove fracture propagation. Fracture height was partially increased in the newly initiated parts of the fracture. The high permeability zone exhibiting higher total stresses above the initiated fracture represented again the vertical limit in the upward direction.

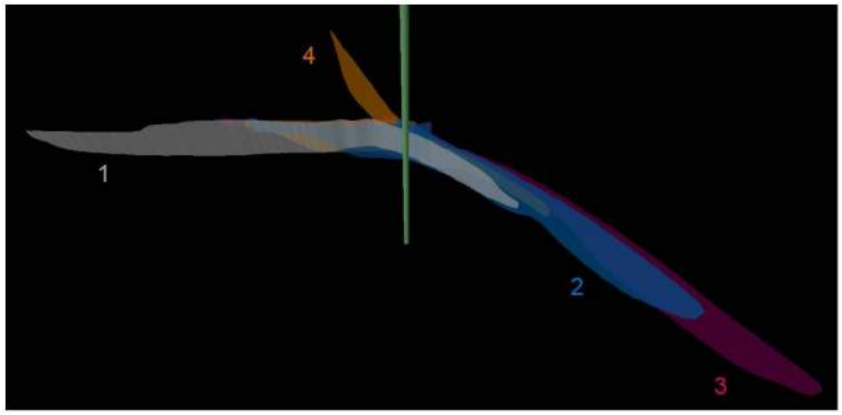

Figure 22—Summary of the hydraulic fracture development in the polymer scenario showing the fracture generation and propagation in the four time steps considered.

Following strong initial propagation, the fracture was only partially re-opened and a new minor fracture developed marking the stabilization in the same way as in the previous scenario. Fig. 22 summarizes the fracture development in this scenario.

Scenario 4: Water injection into oil leg after previous production period. The fourth scenario considered a production period of three years, after which the producer was turned into a water injector. The BHP development together with production and injection rates are shown in Fig. 23. Regarding formation saturation, injection rates and injected fluid, this scenario was very similar to the oil-leg (second) scenario. The difference lay in the production period preceding injection and the first time step at the start of injection. Especially the depletion period resulted in significantly different conditions to be evaluated for fracturing potential. The most important time step in this scenario was therefore the time at maximum depletion when injection started. Because the oil-leg scenario covered the more long-term fracture behavior with its time steps, the additional time steps in this scenario focused on the first month after the start of injection.

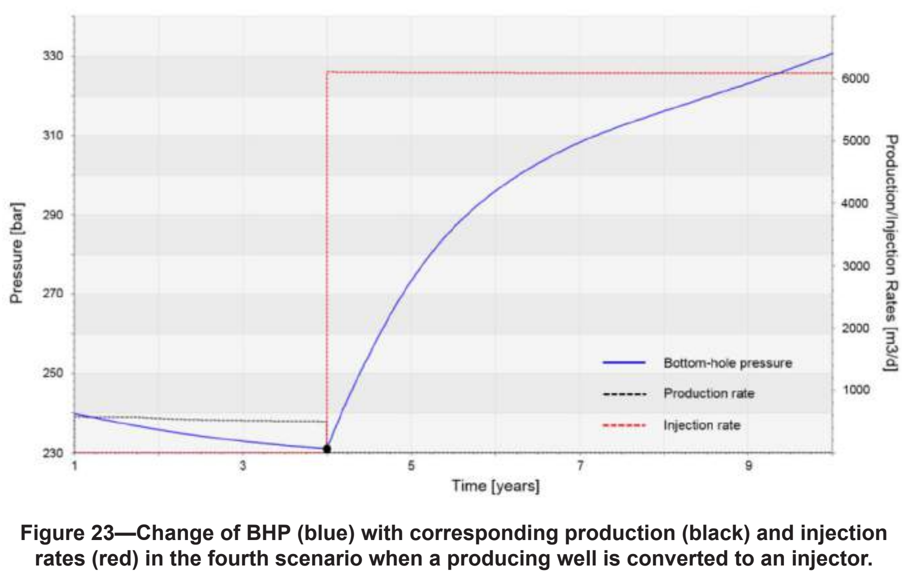

Figure 23—Change of BHP (blue) with corresponding production (black) and injection rates (red) in the fourth scenario when a producing well is converted to an injector.

The depletion of reservoir pressure of up to 140 bar over 3 years was followed by a rapid increase in reservoir pressure of up to 170 bar in the first month. Both types of pressure changes were concentrated on the high permeability zones of the reservoir, but whereas the low production rates yielded a more widespread depletion signature, the high injection rates resulted in much sharper pressure change in these intervals.

The hydraulic fracture simulation was run for the first time step representing the time of maximum depletion. The simulation results are summarized in Fig. 24. The results showed that an initial hydraulic fracture was likely to be generated in the upper part of the reservoir. The point of fracture initiation was located directly above the central zone of high permeability, in a layer of low effective permeability and low minimum horizontal stress. A primary hydraulic fracture was likely to be initiated at this start of injection with a length of about 100 m and a height of 15 m.

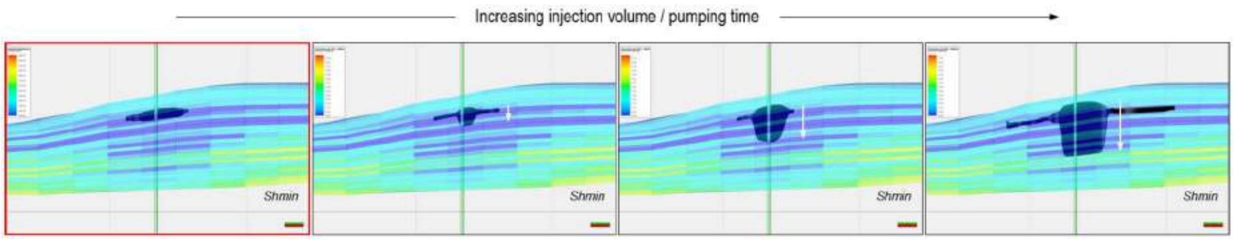

Figure 24—Initial fracture development in the fourth scenario after the producing well is turned into an injector showing downward fracture growth with increasing injection volume and time.

Increasing injection volumes and correspondingly extended pumping times resulted in the fracture propagating vertically downward into the depleted, low-stress zone. Upward propagation was limited by a ayer comprising a higher stress state at the top of the reservoir.

The initial fracture was upscaled to the reservoir grid and used to modify the fluid flow simulation. The hydraulic fracture simulations for the following time steps were then performed with updated reservoir conditions. Fig. 25 summarizes the results for the second, third, and fourth time step.

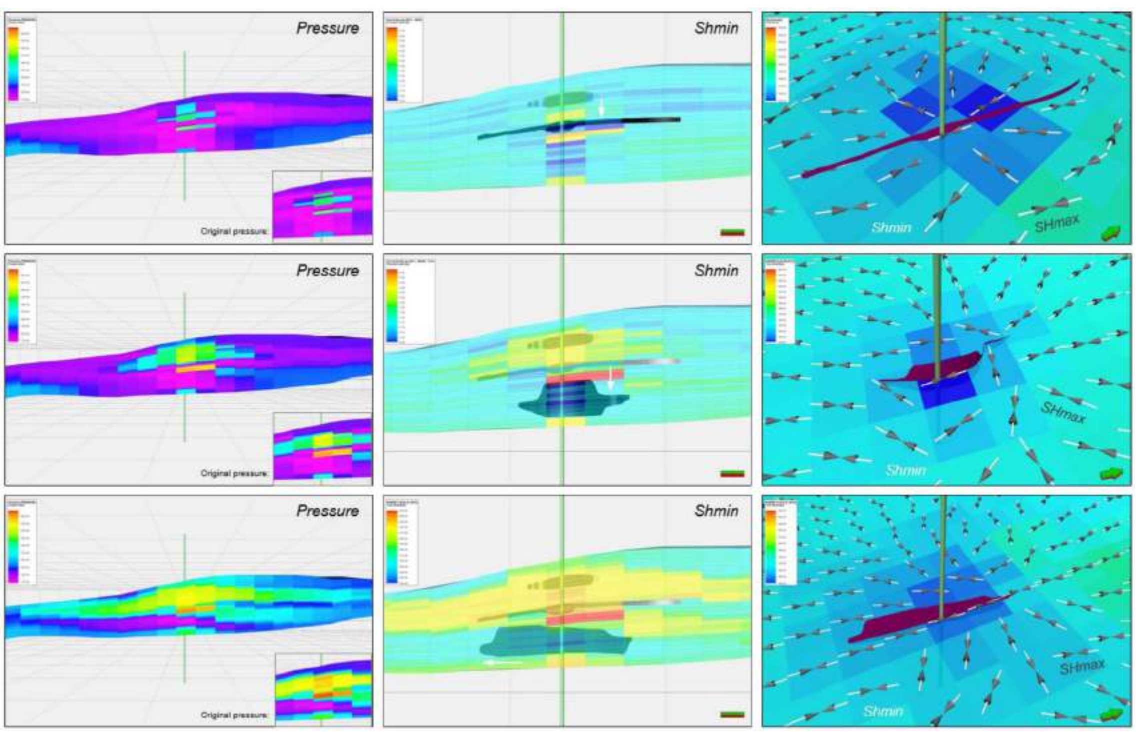

Figure 25—Fracture development in the second (top row), third (center row) and fourth (bottom row) time step (i.e. iteration of the workflow cycle) in the fourth scenario. The results show a consecutive downward shifting of new fracture initiation, which is displayed in context with the reservoir pressure (left column), Shmin magnitude (center column), and the SHmax trajectories (right column).

Instead of re-opening and propagating the initial fracture, the hydraulic fracture simulation results for these subsequent time steps showed the initiation of a new fractures in the low permeability zones in the center and lower part of the reservoir below the initial fracture (Fig. 25). This downward shift of fracturing appeared to be driven by the change in stress.

The final fracture in the lower zone was likely to further grow to a similar size as in the oil-leg (second) scenario. Since the stress field and its in-situ orientation was changing during the time steps and depth intervals, the fractures developed in accordingly aligned orientations. The fracture generated in the lower section of the reservoir showed a significantly larger height growth due to the wider zone of low stress.

The results of this scenario overall indicated that at the start of injection into the previously depleted reservoir, fracture initiation was likely to occur at the start of injection in the upper part of the reservoir, where the combination of low effective permeability and low stress was most favorable. Under the given conditions, the stress state at the very top of the reservoir prevented the hydraulic fracture from propagating upward out of the reservoir. After initial fracture generation, the simulation results suggest a downward movement of fracture development. The fracture initiated and propagated in this lower section of the reservoir was vertically limited by the build-up stress barrier above.

Discussion

This study was carried out within a research project and represents a proof of concept. The staggered nature of the workflow requires the assumption that hydraulic fracture initiation and propagation are rather instantaneous processes than slowly progressing, continuous developments. In other words, an initial hydraulic fracture is generated rapidly when the breakdown limit is reached and propagates periodically afterwards every time the pressure build-up exceeds the fracture's stability. This assumption is justifiable in particular in the scenarios of produced water reinjection when fracturing will be significantly driven by successive permeability reduction due to injected solids.

The main limitation of the workflow currently lies in the turnaround time of the workflow cycle and the selection of time steps at which fracture initiation and propagation is tested and simulated. The precision of this selection could be increased by a closer connection between the hydraulic fracturing simulator and the fluid flow and geomechanical simulators. This would also reduce the turnaround time to less than hour per cycle.

For this study, the injecting well was assumed to be vertical to facilitate the prototype workflow assessment. However, the workflow can be also applied to deviated and horizontal wells and considering the actual trajectory of the deviated well instead of a vertical version would also improve the history match confidence. Depending on the in-situ stress state, the deviated trajectory may change the fracture development significantly.

In the industry, laboratory test data on formation damage and consequent permeability reduction are usually absent or lack completeness. Furthermore, the increase in the well injectivity due to multiple induced hydraulic fractures needs to be validated. Therefore, a history matching process is strongly recommended to adjust and validate the parameters of the permeability reduction model.

It would also be important to properly consider the possibility of heterogeneously distributed damage from drilling and completion, which may influence rate of plugging on matrix bed filtration, time to fracturing, and location of fracture initiation. Initial injectivity, pressure transient data, and production logs may help to better characterize the wellbore and match the well history, therefore improving the permeability reduction and hydraulic fracturing modeling.

Conclusions

The established workflow was successfully applied and offers insights into the hydraulic fracture development in a heterogeneous, yet conventional, reservoir in a new degree of detail for different conditions during produced water re-injection. The study demonstrates that commercially available, state-of-the-art simulators can be combined in a coupling scheme that allows us to obtain specific fracture geometries that respond to changes in stress and petrophysical properties. Despite the limitations and assumptions of the workflow, it has advantages over more traditional modeling approaches. Its main advantage is the amount of complexity being considered, which includes heterogeneity of reservoir properties and changes in fluid saturation, pressure and stress, as well as permeability reduction due to formation damage.

Results show that under the given conditions and assumptions, hydraulic fracturing is unlikely to occur during the injection of water into a water-saturated formation. The injection of both water and polymer into an oil-saturated formation is likely to induce hydraulic fractures of considerable length that are propagated first before the fracture development stabilizes. The difference in viscosity between the injected water and polymer resulted mainly in different timing of events and fracture height, with the polymer scenario showing a more rapid development and more pronounced height growth. These hydraulic fractures are most likely generated in the lower part of the reservoir within intervals of low permeability and are vertically bound by a stress barrier developing during injection in the high-permeability zones above.

The results also show that when a producer is converted into a water injector after years of production, a hydraulic fracture is likely to be initiated at the start of injection in the upper part of this reservoir. At the given conditions, the in-situ stress field drives the propagation of the initial fracture, as well as the additional fractures, downwards to lower intervals of the reservoir. The stress barrier developing in the high-permeability zones limits vertical fracture propagation. Ramping up injection rates after the conversion of a previously producing well will help to minimize the risk of early fracture propagation into the cap rock.

Besides addressing eventual reservoir integrity concerns, the established workflow may also be used to predict in detail the positive or negative impact of the induced fractures on the field oil production, which can be used to guide operational decisions.

Acknowledgments

The authors would like to thank the Agencia Nacional do Petroleo, ANP, for their support to the research initiatives for the petroleum industry of Brazil. They are also grateful to Statoil ASA, for their support, valuable contributions, and data release. The authors would also like to thank Marcelo Frydman, Scientific Advisor, Austin Boyd, BRGC Research Director, and Adrian Rodriguez-Herrera, Geomechanics Technology Program Lead in Schlumberger, for their support, helpful comments, and suggestions.

Nomenclature

C_{ads} = *concentration of adsorbed particles onto the rock surface*
C_{maxads} = *maximum concentration of adsorbed particles onto the rock surface*
C_{sol} = *suspended particle concentration in the diluted and the injected water*
K_{abs} = *absolute permeability*
K_{eff} = *fluid effective permeability*
K_{eq} = *equivalent permeability*
K_{frac} = *hydraulic fracture permeability*
K_{intact} = *intact rock permeability*
$K_{roworig}$ = *original oil relative permeability*
K_{rowads} = *oil relative permeability after particle adsorption*
K_{red} = *reduced absolute permeability*
K_{rw} = *water relative permeability*
K_{rwads} = *water relative permeability after particle adsorption*
$K_{rwmaxads}$ = *water relative permeability after maximum particle adsorption*
K_{rworig} = *original water relative permeability*

RRF = *residual resistance factor*
RRF_{max} = *maximum residual resistance factor*

References

Ali, A.H.A., Brown, T., Delgado, R. et al. 2003. Watching Rocks Change – Mechanical Earth Modeling. *Oilfield Review* **15** (2): 22–39.

Bedrikovetsky, P., Marchesin, D., Shecaira, F. et al. 2001. Characterisation of Deep Bed Filtration System from Laboratory Pressure Drop Measurements. *J. Pet. Sci. Eng.* **32**: 167–177. http://dx.doi.org/10.1016/s0920-4105(01)00159-0.

Cohen, C. E., Kresse, O., and Weng, X. 2015. A New Stacked Height Growth for Hydraulic Fracturing Simulation. 49th US Rock Mechanics/Geomechanics Symposium San Francisco, California, USA, 28 June–1 July. ARMA-2015-073.

Dershowitz, B., LaPointe, P., Eiben, T. et al. 2000. Integration of Discrete Feature Network Methods with Conventional Simulator Approaches. *SPE Reservoir Eval. & Eng* **3** (2): 165–170. SPE-62498-PA. http://dx.doi.org/10.2118/62498-PA.

Farajzadeh, R. 2004. *Produced Water Re-Injection (PWRI): An Experimental Investigation into Internal Filtration and External Cake Build Up*. MSc. Thesis, Delft University of Technology, Delft.

Fjaer, E., Holt, R.M., Horsrud, P., et al. 2008. *Petroleum Related Rock Mechanics*, second edition. Elsevier.

Frydman, M. and Ramirez, H.A. 2006. Using Breakouts for In Situ Stress Estimation in Tectonically Active Areas. 41st U.S. Symposium on Rock Mechanics, Golden, Colorado, USA, 17–21 June. ARMA-06-985.

Heffer, K., Greenhough, J., Main, G. et al. 2010. Low-cost monitoring of inter-well reservoir communication paths through correlations in well rate fluctuations: case studies from mature fields in the North Sea. SPE EUROPEC/EAGE Annual Conference and Exhibition, 14–17 June, Barcelona, Spain. SPE 130734.

Herwanger, J. and Koutsabeloulis, N. 2011. *Seismic Geomechanics: How to Build and Calibrate Geomechanical Models using 3D and 4D Seismic Data (EET 5)*. EAGE Publications.

Koutsabeloulis, N. and Rylance, M. 1992. On the Integration of Multi-Laminate Model for Soils. 4th International Symposium on Numerical Models in Geomechanics, NUMOG IV. Swansea, UK.

Kresse, O., Weng, X., Wu, R. et al. 2012. Numerical Modeling of Hydraulic Fractures Interaction in Complex Naturally Fractured Formations. 46th US Rock Mechanics/Geomechanics Symposium. Chicago, Illinois, USA, 24–27 June. ARMA 12-292.

Mohamad Hussein, A., Minton, J., Rawnsley, N. et al. 2010. Coupled Reservoir Geomechanical Modeling of a Thermal Gas Oil Gravity Drainage Project. SPE EOR Conference, Muscat, Oman. 11–13 April. SPE 127822.

Pande, G. N., Beer, G., and Williams, J. R. 1990. *Numerical Methods in Rock Mechanics*. West Sussex, England. John Wiley and Sons.

Pang, S. and Sharma, M.M. 1994. A Model for Predicting Injectivity Decline in Water-Injection Wells. *SPE Form Eval* **12** (3): 194–201. SPE-28489-PA. http://dx.doi.org/10.2118/28489-PA.

Plumb, R.A., Hooyman, P., Veeningen, D. et al. 2004. A New Geomechanics Process Reduces Operational Risk from Exploration to Production. 6th North America Rock Mechanics Symposium, Houston, Texas, USA, 5–9 June. ARMA-04-616.

Soo, H. and Radke, C.J. 1986. A Filtration Model for the Flow of Dilute, Stable Emulsions in Porous Media – 1. *Theory. Chem. Eng. Sci.* **41** (2): 263–272. http://dx.doi.org/10.1016/0009-2509(86)87007-5.

Weng, X., Kresse, O., Chuprakov, D. et al. 2014. Applying Complex Fracture Model and Integrated Workflow in Unconventional Reservoirs. *Journal of Petroleum Science and Engineering* **124**, 468–483. http://dx.doi.org/10.1016/j.petrol.2014.09.021.

Zhang, X., Koutsabeloulis, N., Kristiansen, T.G. et al. 2011. Modeling of Depletion Induced Micro-Seismic by Coupled Reservoir Simulation: Application to Valhall Field. SPE EUROPEC/EAGE Annual Conference and Exhibition, 23–26 May, Vienna, Austria. SPE 143378.